nature physics

Article

https://doi.org/10.1038/s41567-023-02024-4

Exploiting disorder to probe spin and energy hydrodynamics

Received: 21 December 2022

Accepted: 15 March 2023

Published online: 27 April 2023

Check for updates

Pai Peng [1,6] ✉, Bingtian Ye [2,3,6], Norman Y. Yao [2,3] & Paola Cappellaro [4,5] ✉

An outstanding challenge in large-scale quantum platforms is to simultaneously achieve strong interactions, giving rise to the most interesting behaviours, and local addressing, which can probe them. In the context of correlated phases, local addressing allows one to directly probe the nature of the system's order. At the same time, such addressing allows the study of quantum information spreading and operator growth in out-of-equilibrium scenarios. Here we introduce a technique that enables the measurement of local correlation functions, down to single-site resolution, despite access to only global controls. Our approach leverages the intrinsic disorder present in a solid-state spin ensemble to dephase the non-local components of the correlation function. Utilizing this toolset, we measure both the spin and energy transport in nuclear spin chains. By tuning the interaction Hamiltonian via Floquet engineering, we investigate the cross-over between ballistic and diffusive hydrodynamics. Interestingly, in certain parameter regimes, we observe the coexistence of diffusive spin transport with ballistic energy transport, a hallmark of interacting integrable systems.

The complex dynamics of isolated quantum many-body systems are often amenable to a simple yet powerful description given by classical hydrodynamics[1–6]. However, characterizing the nature of these hydrodynamical descriptions[7–17] and how they emerge from microscopic quantum dynamics remains an area of active pursuit[18–26]. Recently, this pursuit has seen tremendous advances owing to the development of large-scale quantum simulation platforms ranging from ultracold atoms and superconducting circuits, to solid-state spin systems[27–31].

To control and probe many-body dynamics in such systems, one typically requires a combination of strong interactions and local manipulation. In the majority of platforms, these two features are in tension: strong interactions arise when the constituent degrees of freedom are closely spaced, which in turn challenges the ability to perform local measurements[32–34]. The tension is particularly acute in solid-state platforms where electronic and nuclear spins can exhibit strong interactions only when spaced at nanometre length scales. Here, we demonstrate that disorder, often times unavoidable in solids and long-considered detrimental for quantum coherence and transport, can be a powerful source of local control. First, by dephasing a homogenous state using the disorder, we demonstrate the preparation of states whose polarization on different sites is uncorrelated. Second, we show that single-site, spin–spin correlation functions can be directly measured using spin echo. The intuition behind our approach is the following—owing to the lack of spatial correlations, non-local components of the correlation function are averaged out, leaving only a sum of autocorrelations. Applying our technique in the context of nuclear magnetic resonance, we demonstrate the direct observation and characterization of nanoscale spin and energy transport, without the need for magnetic field gradients, subdiffraction techniques or multiple spin species[28,35–40].

Our experiments are performed on $S = 1/2$ ^{19}F nuclear spins within a single crystal of fluorapatite. The nuclear spins effectively form quasi-one-dimensional (1D) chains, since the interchain couplings are ~40 times weaker than the intrachain couplings (Fig. 1a). We place

[1]Department of Electrical Engineering and Computer Science, Massachusetts Institute of Technology, Cambridge, MA, USA. [2]Department of Physics, University of California, Berkeley, CA, USA. [3]Department of Physics, Harvard University, Cambridge, MA, USA. [4]Department of Nuclear Science and Engineering, Massachusetts Institute of Technology, Cambridge, MA, USA. [5]Research Laboratory of Electronics, Massachusetts Institute of Technology, Cambridge, MA, USA. [6]These authors contributed equally: Pai Peng, Bingtian Ye. ✉e-mail: paipeng@mit.edu; pcappell@mit.edu

https://doi.org/10.1038/s41567-023-02024-4

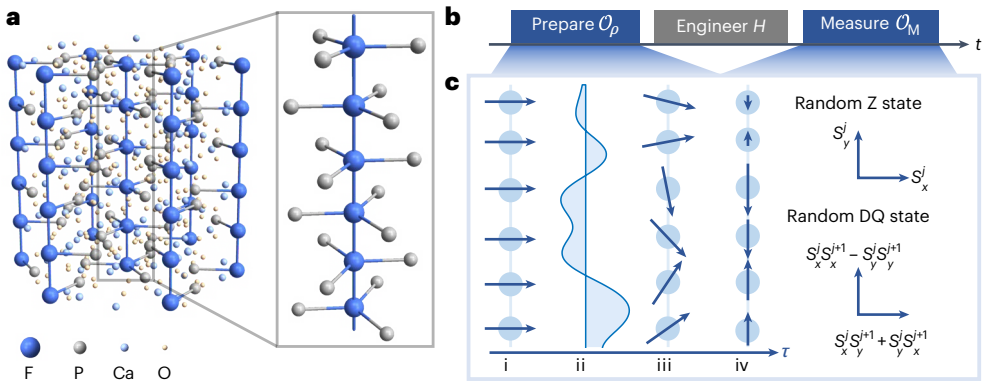

Fig. 1 | Measuring local autocorrelations by utilizing global control and intrinsic on-site disorder. a, Chemical structure of Fluorapatite. ^{19}F nuclear spins (blue balls) form a quasi-1D structure and can exhibit different classes of hydrodynamics under various effective Hamiltonians realized by Floquet engineering. ^{31}P atoms (grey) provide intrinsic on-site disordered fields on ^{19}F spins, which enables the preparation of random states and observables. **b**, The experimental protocol to obtain local autocorrelations consists of three main stages. The central ingredient is to realize spatially uncorrelated random states and observables in the preparation and the measurement stages. Hamiltonian engineering enables the varying of the quantum dynamics. **c**, The sequence to prepare random states and observables contains four steps: (i) initialize the system to a spatially homogeneous state with polarization along the x axis, (ii) apply a disordered field along the z axis to encode (iii) local information into the spin phases and (iv) perform phase cycling to eliminate the residual homogeneous part. The arrows represent spin operators whose bases are specified on the right for the random Zeeman (Z) state and the random DQ state, respectively. To effectively measure spatially random observables, we apply the same sequence in reverse order to the final state before measuring the homogeneous magnetization.

our sample in a 7 T magnetic field along the [001] axis, which leads to a strong Zeeman splitting that reduces the dipolar interaction between ^{19}F spins to its secular form,

$$H_{\mathrm{FF}} = \sum_{j<k} \frac{J}{2r_{jk}^3}\left(2S_z^jS_z^k - S_x^jS_x^k - S_y^jS_y^k\right), \tag{1}$$

where $J = 30.4$ krad s^{-1} and r_{jk} is the distance between sites j and k (measured in units of the lattice constant). The presence of ^{31}P nuclear spin-1/2's leads to additional Ising interactions, $H_{\mathrm{FP}} = \sum_{j,k} J_{jk}^{\mathrm{FP}} S_z^j I_z^k / r_{jk}^3$, where I_z^k is the spin operator of ^{31}P and J_{jk}^{FP} includes the angular dependence of the dipole–dipole coupling (Methods). Crucially, the ^{31}P nuclear spins are randomly polarized at room temperature and their interaction strength is significantly weaker than both H_{FF} and H_{FP}; to this end, I_z^k can be approximated as a scalar random variable, which effectively plays the role of a static, on-site disorder field for the ^{19}F spins:

$$H_{\mathrm{dis}} = \sum_j w_j S_z^j, \tag{2}$$

where w_j is drawn from a Gaussian distribution with an estimated width of 6 krad s^{-1} (Methods and Extended Data Fig. 1).

To probe the infinite-temperature transport of spin and energy in our system, one must measure autocorrelation functions of the form $\sim \mathrm{Tr}[S_z^j(t)S_z^j(0)]$. To do so, we begin by evolving a weakly polarized thermal state $\rho_0 \propto (\mathbb{1} + \epsilon\sum_j S_z^j)$ into a target initial state $\rho \propto \mathbb{1} + \epsilon\mathcal{O}_\rho$. Next, we evolve this initial state under a desired Hamiltonian H for a time t, yielding $\rho(t) = \mathrm{e}^{-\mathrm{i}Ht}\rho\mathrm{e}^{\mathrm{i}Ht}$. Finally, we measure a tunable observable, $\mathcal{O}_{\mathrm{m}}$; in practice, via radiofrequency pulses, this observable is mapped onto the magnetization along the x axis, $\mathcal{M} = \sum_j S_x^j$, which we directly read out via an inductive measurement. The resulting signal is equivalent to the infinite-temperature correlation function, $\mathrm{Tr}[\mathcal{O}_\rho(t)\mathcal{O}_{\mathrm{m}}(0)]$. Clearly, if $\mathcal{O}_\rho$ and $\mathcal{O}_{\mathrm{m}}$ are translationally invariant, the measured signal contains non-local correlations between all pairs of spins, for example $\sum_{jk}\mathrm{Tr}[S_z^j(t)S_z^k(0)]$.

To access local correlation functions, such as the spin survival probability[28,41], we prepare initial states and measure observables such that the spin-polarization at different sites is uncorrelated and averages to zero. An exemplary goal is to prepare and measure the random Zeeman state given by $\mathcal{O}_\rho = \sum_j \alpha_j S_z^j(t)$, where α_j are independent and identically distributed random variables with zero average. This would immediately enable the measurement of sum of single-site autocorrelations since

$$\sum_{j,k}\langle\alpha_j\alpha_k\rangle\mathrm{Tr}[S_z^j(t)S_z^k(0)] \propto \sum_{j,k}\delta_{jk}\mathrm{Tr}[S_z^j(t)S_z^k(0)]$$
$$= \sum_j \mathrm{Tr}[S_z^j(t)S_z^j(0)],$$

which is proportional to single-site autocorrelations $\mathrm{Tr}[S_z^j(t)S_z^j(0)]$ for a translationally invariant Hamiltonian or a disordered Hamiltonian with translationally invariant statistics.

Let us now describe our disorder-based experimental protocol for preparing $\mathcal{O}_\rho$ (Fig. 1c). First, we rotate the thermal polarization to the x axis, initializing a state proportional to $(\mathbb{1} + \epsilon\sum_j S_x^j)$. Then, we evolve under H_{dis} for a time τ, such that the excess magnetization of each spin is oriented along a random direction in the xy plane. To ensure that the time evolution during τ is generated only by H_{dis}, we utilize concatenated WAHUHA sequences (ref. 42) to dynamically decouple H_{FF}. Next, we employ phase cycling to project the random polarization of each spin onto the y axis. A final radiofrequency pulse returns the polarization along z, and we obtain $\mathcal{O}_\rho = \sum_j \alpha_j S_z^j$, with $\alpha_j = \sin(w_j\tau)$ (for additional details see the Supplementary Information Section III). A similar strategy can be used to enable a measurement of $\mathcal{O}_{\mathrm{m}} = \sum_j \alpha_j S_z^j$. In particular, just before the final inductive measurement of $\mathcal{M}$, we refocus the random state back to a uniform magnetization by applying the disorder field again. The above single-site autocorrelation function can be used to detect spin transport. An analogous approach can be used to detect autocorrelations of two-site observables, such as the local energy density. We first use the Jeener–Broekaert pulse pair[43] to create a homogeneous two-body correlated initial state proportional to $\mathbb{1} + \epsilon\sum_j(S_x^jS_y^{j+1} + S_y^jS_x^{j+1})$ (here we assume nearest-neighbour coupling for representation simplicity, but the results also hold with $1/r^3$ long-range coupling; for additional details see the Supplementary Information Section III). Evolution under the disordered field and phase cycling yields the random double-quantum (DQ) state with $\mathcal{O}_\rho = \sum_j \alpha'_j(S_x^jS_x^{j+1} - S_y^jS_y^{j+1})$ where $\alpha'_j = \sin(w_j\tau + w_{j+1}\tau)$ and

https://doi.org/10.1038/s41567-023-02024-4

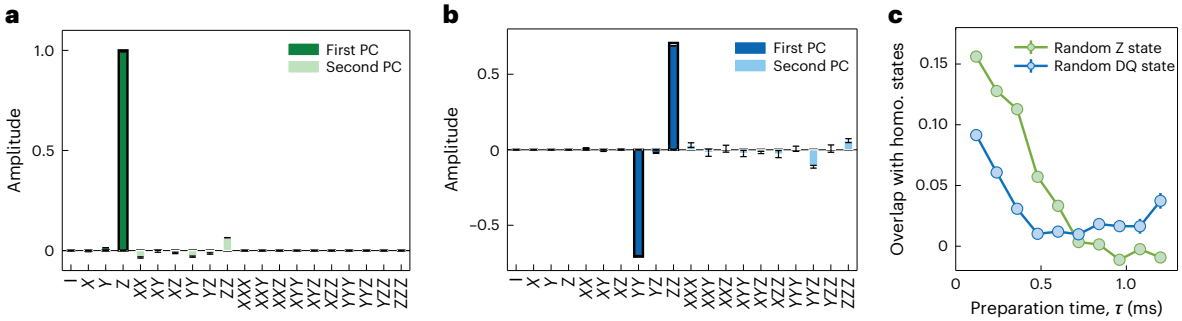

Fig. 2 | Experimental verification of random initial state preparation. a,**b**, The first two principal components (PC) of the experimentally prepared random Zeeman (**a**) and DQ (**b**) states. The horizontal axis label stands for the sum of all permutations of the corresponding spin operators, for example XY corresponds to $\sqrt{2}(S_x^j S_y^{j+1} + S_y^j S_x^{j+1})$ normalized such that the Frobenius norm is 2^L. The amplitude is weighted by the square root of the eigenvalue $\sqrt{\lambda_i}$. For the random Zeeman state, $\lambda_1 = 0.985(1)$, $\lambda_2 = 0.0066(1)$; for the random DQ state, $\lambda_1 = 0.963(9)$, $\lambda_2 = 0.0019(5)$. The eigenvalues are normalized such that $\sum_\mu \lambda_\mu = 1$. The preparation time is 1.08 ms for the random Zeeman state and 0.96 ms for the random DQ state. The green and blue bars show the experimental results, and the black wireframes show the ideal states. **c**, Overlap of the experimentally prepared random Zeeman (green) and DQ (blue) states with the corresponding homogeneous (homo.) state quickly decaying to zero. The overlap of two observables $\mathcal{O}_1$, $\mathcal{O}_2$ is defined as $\mathrm{Tr}(\mathcal{O}_1\mathcal{O}_2)/\sqrt{\mathrm{Tr}(\mathcal{O}_1\mathcal{O}_1)\mathrm{Tr}(\mathcal{O}_2\mathcal{O}_2)}$. Data are presented as mean values ± s.d. from readout noise (for additional details see the Supplementary Information Section V).

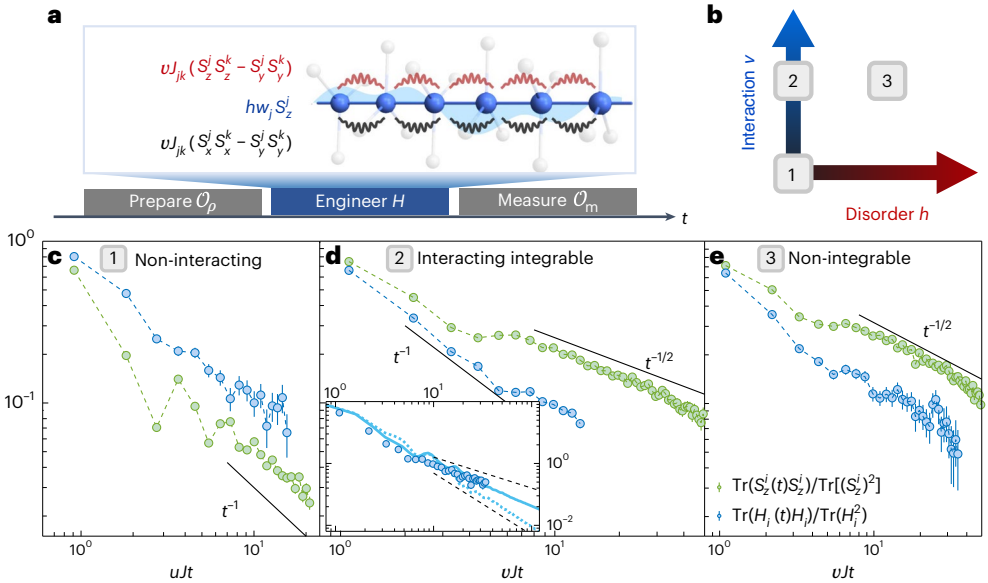

Fig. 3 | Observing different universality classes of hydrodynamics. a, Utilizing Floquet Hamiltonian engineering techniques, we can independently tune the strengths of two types of interactions (red and black wavy lines) and random on-site field (cyan shaded area). Different combinations of the three terms result in distinct classes of Hamiltonian: (1) non-interacting, (2) interacting integrable and (3) non-integrable. **b**, Parameter space of the effective Hamiltonian in equation (3) with varying v, h and fixed u. **c**–**e**, Local autocorrelations of spin and energy in non-interacting (**c**), interacting integrable (**d**) and non-integrable (**e**) systems. All these autocorrelations follow power-law decay $t^{-1/z}$, in which the value of the dynamical exponent z distinguishes between different universality classes. Inset of **d**, the measured energy autocorrelation (dark blue dots) agrees better with the numerical simulation with next-nearest-neighbour coupling (solid curve) than without it (light blue dots), suggesting that the small deviation from ballistic transport at late times is due to the long-range interaction that weakly breaks the integrability of the system. Note that we normalize the local autocorrelations by the corresponding global autocorrelations, except for the spin autocorrelation in the non-interacting case as we do not have access to the collective conserved quantity $\rho = \sum_j (-1)^j S_z^j$. Data are presented as mean values ± s.d. from readout noise (for additional details see the Supplementary Information Section V).

$\langle \alpha_j' \alpha_k' \rangle \propto \delta_{jk}$ for large τ. An additional π/2 pulse naturally realizes $\mathcal{O}_\rho = \sum_j \alpha_j' (S_y^j S_y^{j+1} - S_z^j S_z^{j+1})$. We note that linear combinations of these two initial states allow us to reconstruct all of the subsequent operators we will consider. We can carefully characterize the initial state preparation, focusing on two properties: (i) demonstrating that $\mathcal{O}_\rho$ has support only on the desired operators and (ii) confirming that $\sum \alpha_j = 0$ and $\sum \alpha_j' = 0$. For the first property, we measure $I(\phi, \theta, \gamma) = \mathrm{Tr}[U_r(\phi, \theta, \gamma)\mathcal{O}_\rho U_r^\dagger(\phi, \theta, \gamma)\mathcal{O}_\rho]$ for various $\{\phi, \theta, \gamma\}$, where $U_r = \otimes_j e^{-i\gamma S_z^j} e^{-i\theta S_y^j} e^{-i\phi S_z^j}$. From $I(\phi, \theta, \gamma)$ we can obtain the principal components, $\mathcal{T}_\mu$, of the random observable up to a rotationally invariant component, $\mathcal{O}_\rho = \sum_\mu d_\mu \mathcal{T}_\mu$, where d_μ are independent random variables satisfying $\mathbb{E}(d_\mu d_\nu) = \lambda_\mu \delta_{\mu\nu}$, with λ_μ being the eigenvalues of the correlation matrix in descending order; note that the principal components $\mathcal{T}_\mu$ are orthonormal, $\mathrm{Tr}(\mathcal{T}_\mu \mathcal{T}_\nu^\dagger) = 2^L \delta_{\mu\nu}$. The first two principal components are shown in Fig. 2a,b, confirming our preparation of the random Zeeman state $\mathcal{O}_\rho = \sum_j \alpha_j \sigma_z^j$ and the random DQ state $\mathcal{O}_\rho = \sum_j \alpha_j' (\sigma_x^j \sigma_x^{j+1} - \sigma_y^j \sigma_y^{j+1})$ with high fidelity. As $I(\phi, \theta, \gamma)$ is quadratic in $\mathcal{O}_\rho$, it does not contain information about the sign of the individual random coefficients α_j and α_j'. Therefore, for the second property, we measure the overlap of a random state $\mathcal{O}_\rho$ with its corresponding homogeneous state. As depicted in Fig. 2c, the overlap quickly decays to zero as a function of the preparation time, indicating that, for sufficient

https://doi.org/10.1038/s41567-023-02024-4

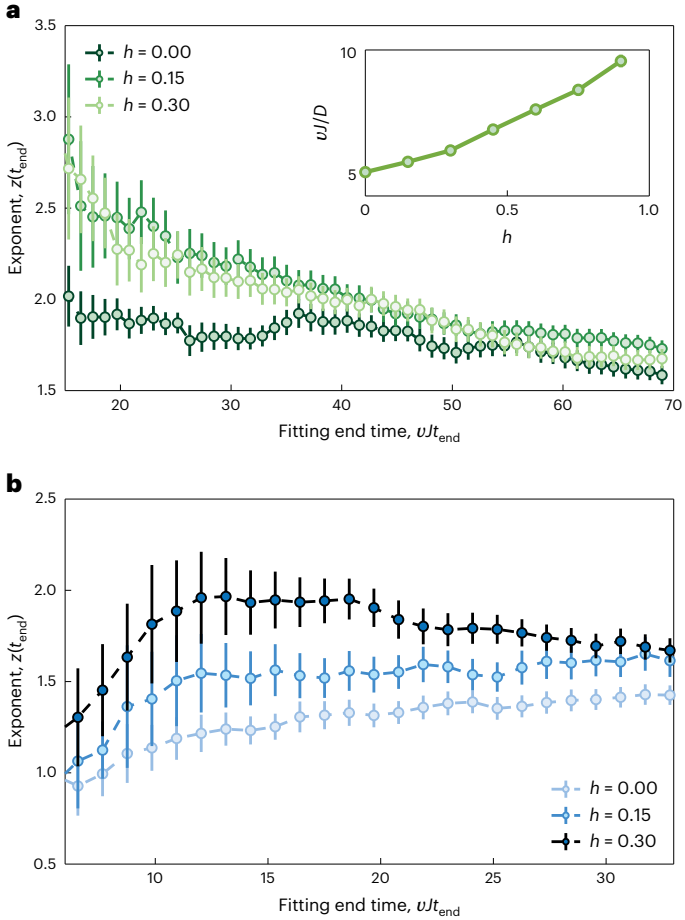

Fig. 4 | Finite-time effect of transport in the presence of an on-site random field. a,**b**, Extracted dynamical exponent of spin (**a**) and energy (**b**) transport in different fitting time windows. The fitting window starts after the transient dynamics (Jt_{start} = 7.7 for **a** and Jt_{start} = 2.2 for **b**); note that the qualitative features we observed do not depend on this specific choice. Inset of **a**, inverse of the diffusion constant D extracted by fitting the data from Jt_{start} = 7.7 to Jt_{end} = 60.0, with υ = 0.3 and a = 3.442 Å the fluorapatite lattice constant. Data are presented as mean values ± s.d. from fitting.

time evolution under the disordered field, one naturally realizes $\mathbb{E}\alpha_j = \mathbb{E}\alpha'_j = 0$.

Probing emergent spin and energy hydrodynamics

Having verified our initial state preparation, we now turn to exploring the infinite-temperature transport of both spin and energy for three distinct classes of Hamiltonians (Fig. 3b): (1) non-interacting integrable, (2) interacting integrable and (3) non-integrable. Utilizing Floquet engineering, we build each of these Hamiltonians from the native dipolar interaction[44,45]. In particular, our experiments enable the realization of the following tunable model,

$$\begin{aligned} H = & u\sum_{j<k}\frac{J}{r_{jk}^3}\left(S_x^jS_x^k - S_y^jS_y^k\right) \\ & +\upsilon\sum_{j<k}\frac{J}{r_{jk}^3}\left(S_z^jS_z^k - S_y^jS_y^k\right) \\ & +h\sum_j w_jS_z^j, \end{aligned} \tag{3}$$

where the coefficients $\{u, \upsilon, h\}$ can be independently controlled. For $\{\upsilon, h\} = 0$ and restricting to nearest-neighbour couplings (that is, truncating the long-range dipolar tail), the resulting XY model is integrable and free (case 1). Upon adding non-zero υ, the model remains integrable, but becomes interacting (case 2). Finally, the addition of a weak on-site random field, h, causes the model to generically become non-integrable (case 3). We note that the long-range nature of the dipolar interaction renders H generically non-integrable for all of the above cases. However, our hope is that signatures of integrability will be present in the dynamics at short times; as we will see below, this is indeed borne out by the data.

These three different universality classes can be distinguished by the dynamical exponent, z, associated with their spin and energy transport. Crucially, z can be directly measured via the power-law decay of the autocorrelation function $\sim t^{-1/z}$, with $z = 1$ corresponding to ballistic motion and $z = 2$ corresponding to diffusion.

Let us begin with case 1. We tune $\{u, \upsilon, h\} = \{0.5, 0, 0\}$ and measure the spin–spin autocorrelation function (Fig. 3c, green) and the energy autocorrelation function (Fig. 3c, blue). Both exhibit late-time power laws consistent with $z = 1$, in agreement with the expectation that quasiparticles propagate ballistically in a non-interacting, integrable model. For case 2, we tune our system to $\{u, \upsilon, h\} = \{-0.15, 0.3, 0\}$. Intriguingly, we find that spin transports diffusively while energy transports ballistically (Fig. 3d). This phenomenon is due to the existence of stable spinless quasiparticles and is a central feature of infinite-temperature transport in the so-called XXZ model[22,23,46–53]. Finally, for case 3, we set $\{u, \upsilon, h\} = \{-0.15, 0.3, 0.23\}$ and observe that both spin and energy transport diffusively (Fig. 3e), consistent with a generic non-integrable model[4,26]. The maximum time explored here is limited by the interchain coupling, which, albeit being 40 times smaller than intrachain coupling, becomes non-negligible at $\upsilon Jt \approx 50$ and breaks the quasi-1D approximation.

Two remarks are in order. First, the energy transport data in case 2 exhibit a weak deviation from ballistic transport at the longest times explored in the experiment (inset, Fig. 4d). To understand the origin of this deviation, we numerically compute the energy autocorrelation function in a 1D spin chain using density matrix truncation, with and without long-range couplings[11]. The agreement between our experiment and numerics in the former case suggests that the observed deviation results from the weak breaking of integrability associated with the long-range intrachain couplings, which is eight times weaker than the nearest-neighbour interaction. Second, by tuning the disorder strength during the evolution, we can controllably break integrability and access the non-integrable regime on the experimental timescale. In Fig. 4, we measure the energy and spin transport as we tune h from 0 to 0.3 (Methods and Extended Data Fig. 2). We extract z using different time windows of the autocorrelation function, starting at $t_{start} = 7.7/J$ and ending at a variable t_{end}. For the spin transport (Fig. 4a), after an initial transient, all of the models exhibit a $z = 2$ at intermediate times. At the latest times, the interchain couplings begin to play a role, causing a decrease in z. Meanwhile, for the energy transport at $h = 0$, z remains close to its initial ballistic value for all times. However, for $h = 0.3$, the system reaches a diffusive exponent ($z = 2$) at intermediate times before exhibiting a weak decrease (possibly owing to interchain couplings).

In summary, our results introduce a new method to probe local spin and energy transport in solid-state spin ensembles. Our technique leverages the intrinsic disorder in such systems and requires only collective control. Our local probe enables exploration of quantum many-body phenomena unavailable in homogeneous systems, such as the ballistic and diffusive hydrodynamics demonstrated here, or subdiffusion near the many-body localization transition and the emergence of superdiffusion with long-range interactions[18,31,54–58]. In addition to two-point correlation functions, which were the focus of the present work, our protocols can naturally be generalized to four-point, out-of-time-ordered correlations, and thus used to probe many-body quantum information scrambling[59–70]. Beyond quantum simulation, transport measurements provide rich information of the system, and therefore can also boost quantum sensing applications in material and biological science. Finally, we point out that a general static

inhomogeneous field can similarly induce the dephasing process and thus create random states, broadening the application of the present scheme to quantum platforms where disorder is not naturally present, including cold atoms, trapped ions and superconducting circuits.

Online content

Any methods, additional references, Nature Portfolio reporting summaries, source data, extended data, supplementary information, acknowledgements, peer review information; details of author contributions and competing interests; and statements of data and code availability are available at https://doi.org/10.1038/s41567-023-02024-4.

References

1. Halliwell, J. Decoherent histories and the emergent classicality of local densities. *Phys. Rev. Lett.* **83**, 2481–2485 (1999).
2. Wyatt, R. E. *Quantum Dynamics with Trajectories: Introduction to Quantum Hydrodynamics* Vol. 28 (Springer Science & Business Media, 2005).
3. Hartle, J. B. The quasiclassical realms of this quantum universe. *Found. Phys.* **41**, 982–1006 (2011).
4. Spohn, H. *Large Scale Dynamics of Interacting Particles* (Springer Science & Business Media, 2012).
5. Birkhoff, G. in *Hydrodynamics* (Princeton University Press, 2015).
6. De Nardis, J., Bernard, D. & Doyon, B. Hydrodynamic diffusion in integrable systems. *Phys. Rev. Lett.* **121**, 160603 (2018).
7. Andreev, A., Kivelson, S. A. & Spivak, B. Hydrodynamic description of transport in strongly correlated electron systems. *Phys. Rev. Lett.* **106**, 256804 (2011).
8. Žnidarič, M., Scardicchio, A. & Varma, V. K. Diffusive and subdiffusive spin transport in the ergodic phase of a many-body localizable system. *Phys. Rev. Lett.* **117**, 040601 (2016).
9. Bertini, B., Collura, M., De Nardis, J. & Fagotti, M. Transport in out-of-equilibrium x x z chains: exact profiles of charges and currents. *Phys. Rev. Lett.* **117**, 207201 (2016).
10. Leviatan, E., Pollmann, F., Bardarson, J. H., Huse, D. A. & Altman, E. Quantum thermalization dynamics with matrix-product states. Preprint at arXiv:1702.08894 (2017).
11. Ye, B., Machado, F., White, C. D., Mong, R. S. & Yao, N. Y. Emergent hydrodynamics in nonequilibrium quantum systems. *Phys. Rev. Lett.* **125**, 030601 (2020).
12. Ljubotina, M., Žnidarič, M. & Prosen, T. Kardar-Parisi-Zhang physics in the quantum Heisenberg magnet. *Phys. Rev. Lett.* **122**, 210602 (2019).
13. Ye, B., Machado, F., Kemp, J., Hutson, R. B. & Yao, N. Y. Universal Kardar-Parisi-Zhang dynamics in integrable quantum systems. *Phys. Rev. Lett.* **129**, 230602 (2022).
14. Sommer, A., Ku, M., Roati, G. & Zwierlein, M. W. Universal spin transport in a strongly interacting Fermi gas. *Nature* **472**, 201–204 (2011).
15. Moll, P. J., Kushwaha, P., Nandi, N., Schmidt, B. & Mackenzie, A. P. Evidence for hydrodynamic electron flow in $PdCoO_2$. *Science* **351**, 1061–1064 (2016).
16. Cepellotti, A. et al. Phonon hydrodynamics in two-dimensional materials. *Nat. Commun.* **6**, 6400 (2015).
17. Crossno, J. et al. Observation of the dirac fluid and the breakdown of the wiedemann-franz law in graphene. *Science* **351**, 1058–1061 (2016).
18. Agarwal, K., Gopalakrishnan, S., Knap, M., Müller, M. & Demler, E. Anomalous diffusion and griffiths effects near the many-body localization transition. *Phys. Rev. Lett.* **114**, 160401 (2015).
19. Castro-Alvaredo, O. A., Doyon, B. & Yoshimura, T. Emergent hydrodynamics in integrable quantum systems out of equilibrium. *Phys. Rev. X* **6**, 041065 (2016).
20. Bertini, B. Finite-temperature transport in one-dimensional quantum lattice models. *Rev. Mod. Phys.* **93**, 025003 (2021).
21. Ilievski, E. & De Nardis, J. Microscopic origin of ideal conductivity in integrable quantum models. *Phys. Rev. Lett.* **119**, 020602 (2017).
22. Gopalakrishnan, S. & Vasseur, R. Kinetic theory of spin diffusion and superdiffusion in x x z spin chains. *Phys. Rev. Lett.* **122**, 127202 (2019).
23. De Nardis, J., Bernard, D. & Doyon, B. Diffusion in generalized hydrodynamics and quasiparticle scattering. *SciPost Phys* **6**, 049 (2019).
24. Ilievski, E., De Nardis, J., Gopalakrishnan, S., Vasseur, R. & Ware, B. Superuniversality of superdiffusion. *Phys. Rev. X* **11**, 031023 (2021).
25. De Nardis, J., Gopalakrishnan, S., Vasseur, R. & Ware, B. Stability of superdiffusion in nearly integrable spin chains. *Phys. Rev. Lett.* **127**, 057201 (2021).
26. Friedman, A. J., Gopalakrishnan, S. & Vasseur, R. Diffusive hydrodynamics from integrability breaking. *Phys. Rev. B* **101**, 180302 (2020).
27. Schemmer, M., Bouchoule, I., Doyon, B. & Dubail, J. Generalized hydrodynamics on an atom chip. *Phys. Rev. Lett.* **122**, 090601 (2019).
28. Zu, C. et al. Emergent hydrodynamics in a strongly interacting dipolar spin ensemble. *Nature* **597**, 45–50 (2021).
29. Malvania, N. et al. Generalized hydrodynamics in strongly interacting 1d bose gases. *Science* **373**, 1129–1133 (2021).
30. Wei, D. et al. Quantum gas microscopy of Kardar-Parisi-Zhang superdiffusion. *Science* **376**, 716–720 (2022).
31. Joshi, M. K. et al. Observing emergent hydrodynamics in a long-range quantum magnet. *Science* **376**, 720–724 (2022).
32. Martin, L. S. et al. Controlling local thermalization dynamics in a Floquet-engineered dipolar ensemble. Preprint at arXiv:2209.09297 (2022).
33. Altman, E. et al. Quantum simulators: architectures and opportunities. *PRX Quantum* **2**, 017003 (2021).
34. Bakr, W. S., Gillen, J. I., Peng, A., Folling, S. & Greiner, M. A quantum gas microscope for detecting single atoms in a Hubbard-regime optical lattice. *Nature* **462**, 74–77 (2009).
35. Zhang, W. & Cory, D. First direct measurement of the spin diffusion rate in a homogenous solid. *Phys. Rev. Lett.* **80**, 1324 (1998).
36. Rittweger, E., Han, K. Y., Irvine, S. E., Eggeling, C. & Hell, S. W. STED microscopy reveals crystal colour centres with nanometric resolution. *Nat. Photonics* **3**, 144–147 (2009).
37. Maurer, P. et al. Far-field optical imaging and manipulation of individual spins with nanoscale resolution. *Nat. Phys.* **6**, 912–918 (2010).
38. Chen, E. H., Gaathon, O., Trusheim, M. E. & Englund, D. Wide-field multispectral super-resolution imaging using spin-dependent fluorescence in nanodiamonds. *Nano Lett.* **13**, 2073–2077 (2013).
39. Pfender, M., Aslam, N., Waldherr, G., Neumann, P. & Wrachtrup, J. Single-spin stochastic optical reconstruction microscopy. *Proc. Natl Acad. Sci. USA* **111**, 14669–14674 (2014).
40. Arai, K. et al. Fourier magnetic imaging with nanoscale resolution and compressed sensing speed-up using electronic spins in diamond. *Nat. Nanotechnol.* **10**, 859–864 (2015).
41. Hunt, G. A. Some theorems concerning brownian motion. *Trans. Am. Math. Soc.* **81**, 294–319 (1956).
42. Waugh, J. S., Huber, L. M. & Haeberlen, U. Approach to high-resolution nmr in solids. *Phys. Rev. Lett.* **20**, 180–182 (1968).
43. Jeener, J. & Broekaert, P. Nuclear magnetic resonance in solids: thermodynamic effects of a pair of rf pulses. *Phys. Rev.* **157**, 232–240 (1967).
44. Haeberlen, U. & Waugh, J. S. Coherent averaging effects in magnetic resonance. *Phys. Rev.* **175**, 453–467 (1968).
45. Peng, P. et al. Deep reinforcement learning for quantum hamiltonian engineering. *Phys. Rev. Appl.* **18**, 024033 (2022).

46. Grabowski, M. & Mathieu, P. Structure of the conservation laws in quantum integrable spin chains with short range interactions. *Ann. Phys.* **243**, 299–371 (1995).
47. Zotos, X., Naef, F. & Prelovsek, P. Transport and conservation laws. *Phys. Rev. B* **55**, 11029–11032 (1997).
48. Klümper, A. & Johnston, D. Thermodynamics of the spin-1/2 antiferromagnetic uniform Heisenberg chain. *Phys. Rev. Lett.* **84**, 4701–4704 (2000).
49. Sakai, K. & Klümper, A. Non-dissipative thermal transport in the massive regimes of the xxz chain. *J. Phys. A: Math. Gen.* **36**, 11617–11629 (2003).
50. Prosen, T. & Žnidarič, M. Matrix product simulations of non-equilibrium steady states of quantum spin chains. *J. Stat. Mech.: Theory Exp.* **2009**, P02035 (2009).
51. Steinigeweg, R. & Gemmer, J. Density dynamics in translationally invariant spin-1 2 chains at high temperatures: a current-autocorrelation approach to finite time and length scales. *Phys. Rev. B* **80**, 184402 (2009).
52. Žnidarič, M. Spin transport in a one-dimensional anisotropic Heisenberg model. *Phys. Rev. Lett.* **106**, 220601 (2011).
53. Karrasch, C., Moore, J. & Heidrich-Meisner, F. Real-time and real-space spin and energy dynamics in one-dimensional spin-1 2 systems induced by local quantum quenches at finite temperatures. *Phys. Rev. B* **89**, 075139 (2014).
54. Lucioni, E. et al. Observation of subdiffusion in a disordered interacting system. *Phys. Rev. Lett.* **106**, 230403 (2011).
55. Vosk, R., Huse, D. A. & Altman, E. Theory of the many-body localization transition in one-dimensional systems. *Phys. Rev. X* **5**, 031032 (2015).
56. Potter, A. C., Vasseur, R. & Parameswaran, S. Universal properties of many-body delocalization transitions. *Phys. Rev. X* **5**, 031033 (2015).
57. Sahay, R., Machado, F., Ye, B., Laumann, C. R. & Yao, N. Y. Emergent ergodicity at the transition between many-body localized phases. *Phys. Rev. Lett.* **126**, 100604 (2021).
58. Zaburdaev, V., Denisov, S. & Klafter, J. Lévy walks. *Rev. Mod. Phys.* **87**, 483–530 (2015).
59. Nahum, A., Vijay, S. & Haah, J. Operator spreading in random unitary circuits. *Phys. Rev. X* **8**, 021014 (2018).
60. Von Keyserlingk, C., Rakovszky, T., Pollmann, F. & Sondhi, S. L. Operator hydrodynamics, OTOCs, and entanglement growth in systems without conservation laws. *Phys. Rev. X* **8**, 021013 (2018).
61. Rakovszky, T. & Pollmann, F. & Von Keyserlingk, C. Diffusive hydrodynamics of out-of-time-ordered correlators with charge conservation. *Phys. Rev. X* **8**, 031058 (2018).
62. Khemani, V., Vishwanath, A. & Huse, D. A. Operator spreading and the emergence of dissipative hydrodynamics under unitary evolution with conservation laws. *Phys. Rev. X* **8**, 031057 (2018).
63. Xu, S. & Swingle, B. Accessing scrambling using matrix product operators. *Nat. Phys.* **16**, 199–204 (2020).
64. Xu, S. & Swingle, B. Locality, quantum fluctuations, and scrambling. *Phys. Rev. X* **9**, 031048 (2019).
65. Sahu, S., Xu, S. & Swingle, B. Scrambling dynamics across a thermalization-localization quantum phase transition. *Phys. Rev. Lett.* **123**, 165902 (2019).
66. Schuster, T. et al. Many-body quantum teleportation via operator spreading in the traversable wormhole protocol. *Phys. Rev. X* **12**, 031013 (2022).
67. Li, J. et al. Measuring out-of-time-order correlators on a nuclear magnetic resonance quantum simulator. *Phys. Rev. X* **7**, 031011 (2017).
68. Landsman, K. A. et al. Verified quantum information scrambling. *Nature* **567**, 61–65 (2019).
69. Blok, M. S. et al. Quantum information scrambling on a superconducting qutrit processor. *Phys. Rev. X* **11**, 021010 (2021).
70. Wei, K. X. et al. Emergent prethermalization signatures in out-of-time ordered correlations. *Phys. Rev. Lett.* **123**, 090605 (2019).

Methods

Experimental system

The sample in the experiment is a single crystal of fluorapatite with formula $Ca_5(PO_4)_3F$. The most abundant isotopes of F and P have 1/2 nuclear spin, while the most abundant isotopes of Ca and O have zero nuclear spin. Fluorapatite is a hexagonal mineral with space group $P6_3/m$, where the ^{19}F spin-1/2 nuclei form linear chains along the c axis. Each fluorine spin in the chain is surrounded by three equidistant ^{31}P spin-1/2 nuclei. The sample we used is a cut from a natural crystal of approximate dimensions 3 mm × 3 mm × 2 mm. The sample is placed at room temperature inside a superconducting magnet producing a uniform $B = 7$ T field. The total Hamiltonian of the system is given by

$$H_{\mathrm{tot}} = \omega_{\mathrm{F}} \sum_k S_z^k + \omega_{\mathrm{P}} \sum_\kappa s_z^\kappa + H_{\mathrm{dip}} \tag{4}$$

The first two terms represent the Zeeman interactions of the F(S) and P(I) spins, respectively, with frequencies $\omega_{\mathrm{F}} = \gamma_{\mathrm{F}} B \approx (2\pi)282.37$ MHz and $\omega_{\mathrm{P}} = \gamma_{\mathrm{P}} B = (2\pi)121.51$ MHz, where $\gamma_{\mathrm{F/P}}$ are the gyromagnetic ratios. The last term represents the natural magnetic dipole–dipole interaction among the spins, given by

$$\begin{aligned} H_{\mathrm{dip}} &= H_{\mathrm{FF}} + H_{\mathrm{FP}} + H_{\mathrm{PP}} \\ &= \sum_{j<k} \frac{\hbar\gamma_j\gamma_k}{|\mathbf{r}_{jk}|^3} \left[\mathbf{S}_j \cdot \mathbf{S}_k - \frac{3(\mathbf{S}_j\cdot\mathbf{r}_{jk})(\mathbf{S}_k\cdot\mathbf{r}_{jk})}{|\mathbf{r}_{jk}|^2} \right], \end{aligned} \tag{5}$$

where $\mathbf{r}_{jk}$ is the vector between the jk spin pair. Because the Zeeman interaction is much stronger than the dipole–dipole interaction, we can truncate the dipolar Hamiltonian to its energy-conserving part (secular Hamiltonian). We then obtain the homonuclear Hamiltonians

$$\begin{aligned} H_{\mathrm{FF}} &= \frac{1}{2} \sum_{j<k} J_{jk}^{\mathrm{F}} \left(2S_z^j S_z^k - S_x^j S_x^k - S_y^j S_y^k \right) \\ H_{\mathrm{PP}} &= \frac{1}{2} \sum_{\lambda<\kappa} J_{\kappa\lambda}^{\mathrm{P}} \left(2I_z^\lambda I_z^\kappa - I_x^\lambda I_x^\kappa - I_y^\lambda I_y^\kappa \right) \end{aligned} \tag{6}$$

and the heteronuclear interaction between the F and P spins,

$$H_{\mathrm{FP}} = \sum_{k,\kappa} J_{k,\kappa}^{\mathrm{FP}} S_z^k I_z^\kappa, \tag{7}$$

with $J_{jk} = \hbar\gamma_j\gamma_k \frac{1-3\cos(\theta_{jk})^2}{|\mathbf{r}_{jk}|^3}$, where θ_{jk} is the angle between the vector $\mathbf{r}_{jk}$ and the magnetic field z axis. We align the c axis to the 7 T magnetic field. The maximum values of the couplings (for the closest spins) are given by $J = J^{\mathrm{FF}} = -32.76$ krad s^{-1}, $J^{\mathrm{PP}} = 1.20$ krad s^{-1} and $J^{\mathrm{FP}} = 6.12$ krad s^{-1}, respectively. Since the coupling between the ^{31}P spins is much weaker than the others, the dynamics of the ^{31}P spins can be ignored for short times and I only provides a static random field. In addition, as the temperature is much higher than the Zeeman energy, each the ^{31}P spin is randomly polarized with negligible correlation between different ^{31}P spins. As a result, H_{FP} can be viewed as an on-site disordered field for ^{19}F spins

$$H_{\mathrm{dip}} = \frac{1}{2} \sum_{j<k} J_{jk} \left(2S_z^j S_z^k - S_x^j S_x^k - S_y^j S_y^k \right) + \sum_j w_j S_z^j, \tag{8}$$

where $w_j = \sum_\kappa J_{j,\kappa}^{\mathrm{FP}} I_z^\kappa$ is a random number.

The dynamics of this complex three-dimensional many-body system can be mapped to a much simpler, quasi-1D system. First, when the crystal is oriented with its c axis parallel to the external magnetic field the coupling of fluorine spins to the closest off-chain fluorine spin is ≈40 times weaker, while in-chain, next-nearest-neighbour couplings are 8 times weaker. Previous studies on these crystals have indeed observed dynamics consistent with spin chain models, and the system has been proposed as being solid-state realizations of quantum wires[71–73]. This approximation of the experimental system to a 1D, short-range system, although not perfect, has been shown to reliably describe experiments for relevant timescales[74,75]. The approximation breaks down at longer times, with a convergence of various effects: long-range in-chain and cross-chain couplings, as well as pulse errors in the sequences used for Hamiltonian engineering. In addition, the system also undergoes spin relaxation, although on a much longer timescale ($T_1 = 0.8$ s for our sample).

Ab initio calculation of disordered field

The disordered magnetic fields on the ^{19}F originates from the ^{19}F–^{31}P interaction and the random orientation of ^{31}P. This picture allows us to directly calculate the distribution of the disordered field strength. In particular, we compute the interaction strength between ^{19}F and its several closest neighbouring ^{31}P based on their relative position[76] and gyromagnetic ratio. Then we assume each ^{31}P points along the $+z$ or $-z$ direction with the same probability, which effectively applies a magnetic field on ^{19}F along the corresponding direction and with the strength given by the ^{19}F–^{31}P interaction. Summing up the contribution from all ^{31}P gives the total strength of the disorder field. In Extended Data Fig. 1, we include the 45 closest ^{31}P and observe a smooth enough distribution of the field strength. The distribution is perfectly fitted by a sum of four Gaussian distributions with the same width, the centres at $\pm\frac{1}{2}J^{\mathrm{FP}}$ and $\pm\frac{3}{2}J^{\mathrm{FP}}$ and the height ratio of 3:3:1:1. Interestingly, even a single Gaussian function can still capture the distribution reasonably well, so we simply use a Gaussian distribution for simplicity in our numerical simulation. This can be qualitatively justified by comparing the computed T_2 decay profiles of the Gaussian distribution and the true distribution (Extended Data Fig. 1).

Since the disorder fields on different ^{19}F originates from the same ^{31}P bath, they inevitably have some statistical correlation. Here we evaluate the correlation of the disordered fields on two neighbouring ^{19}F, $\frac{\langle w_j w_{j+1}\rangle}{\langle w_j^2\rangle} \approx -0.2$. Nevertheless, $\langle \alpha_j \alpha_{j+1}\rangle = \langle \sin(w_j\tau)\sin(w_{j+1}\tau)\rangle \approx 0$ for $\tau > T_2$ (Extended Data Fig. 1), satisfying the condition required for our protocol to measure local autocorrelation (see Section IV C in the Supplementary Information).

Data for transport with disorder

In Fig. 4 we show the dynamical exponent for various disorder field strengths. We present the source data—autocorrelation as a function of time here—in Extended Data Fig. 2.

Data availability

Source data are provided with this paper. All other data that support the plots within this paper and other findings of this study are available from the corresponding author upon reasonable request.

References

71. Cappellaro, P., Ramanathan, C. & Cory, D. G. Simulations of information transport in spin chains. *Phys. Rev. Lett.* **99**, 250506 (2007).
72. Cappellaro, P., Viola, L. & Ramanathan, C. Coherent-state transfer via highly mixed quantum spin chains. *Phys. Rev. A* **83**, 032304 (2011).
73. Ramanathan, C., Cappellaro, P., Viola, L. & Cory, D. G. Experimental characterization of coherent magnetization transport in a one-dimensional spin system. *New J. Phys.* **13**, 103015 (2011).
74. Rufeil-Fiori, E., Sánchez, C. M., Oliva, F. Y., Pastawski, H. M. & Levstein, P. R. Effective one-body dynamics in multiple-quantum nmr experiments. *Phys. Rev. A* **79**, 032324 (2009).
75. Zhang, W. et al. NMR multiple quantum coherences in quasi-one-dimensional spin systems: comparison with ideal spin-chain dynamics. *Phys. Rev. A* **80**, 052323 (2009).

76. Comodi, P., Liu, Y., Zanazzi, P. & Montagnoli, M. Structural and vibrational behaviour of fluorapatite with pressure. Part I: in situ single-crystal x-ray diffraction investigation. *Phys. Chem. Miner.* **28**, 219–224 (2001).

Acknowledgements

We thank C. Ramanathan, H. Zhou, M. Leigh, N. Leitao, F. Machado, J. Kemp, J. Moore and M. Lukin for helpful conversations. This work was supported in part by the National Science Foundation under grant No. PHY1915218. P.P. thanks MathWorks for their support in the form of a Graduate Student Fellowship. The opinions and views expressed in this publication are from the authors and not necessarily from MathWorks. B.Y. acknowledges support from the Army Research Office through the MURI program (W911NF-20-1-0136). N.Y.Y. acknowledges support from the NSF through the QLCI program (OMA-2016245) and the David and Lucile Packard foundation.

Author contributions

P.P. designed and performed the experiment with assistance from P.C. B.Y. and N.Y.Y. performed the numerical and analytical calculations. P.C. supervised the project. All authors worked on the interpretation of the data and contributed to writing the manuscript.

Competing interests

The authors declare no competing interests.

Additional information

Extended data is available for this paper at https://doi.org/10.1038/s41567-023-02024-4.

Supplementary information The online version contains supplementary material available at https://doi.org/10.1038/s41567-023-02024-4.

Correspondence and requests for materials should be addressed to Pai Peng or Paola Cappellaro.

Peer review information *Nature Physics* thanks Jianming Cai and the other, anonymous, reviewer(s) for their contribution to the peer review of this work.

https://doi.org/10.1038/s41567-023-02024-4

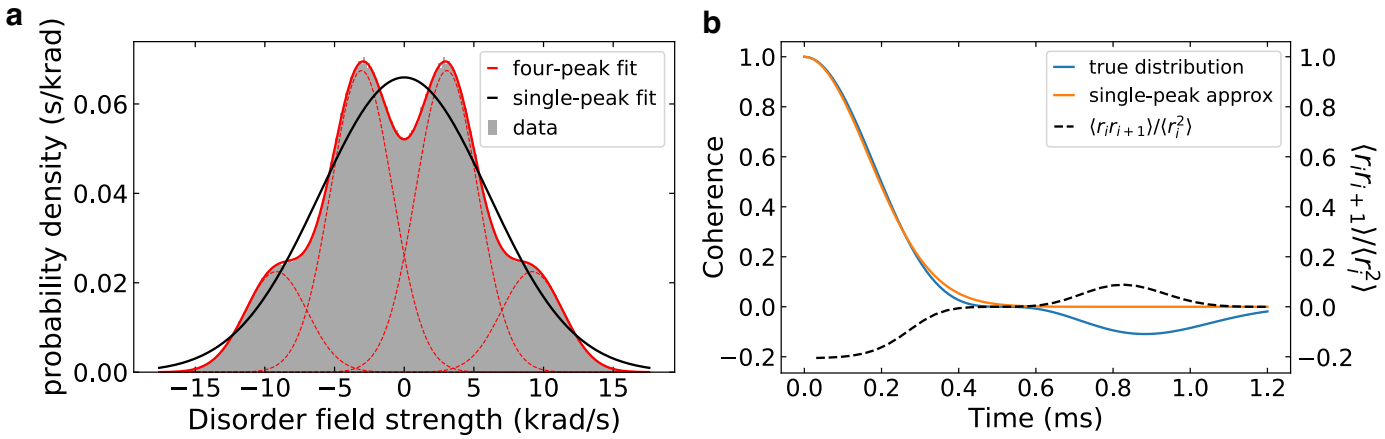

Extended Data Fig. 1 | Ab initio calculation of disordered field and decoherence profile. Disordered on-site field generated by ^{31}P. **a**. Numerical calculation of distribution of the on-site field strength. The four-Gaussian fit gives a standard deviation of 2.217(2) krad/s for each Gaussian peak. The single-Gaussian fit gives a standard deviation of 6.05(6) krad/s. **b**. Left axis: Decoherence profile generated by the calculated distribution of on-site field and the single-peak Gaussian approximation. Right axis: Statistical correlation between the random amplitudes of local observables on two closest ^{19}F. As the coherence approaches zero, the statistical correlation also vanishes.

https://doi.org/10.1038/s41567-023-02024-4

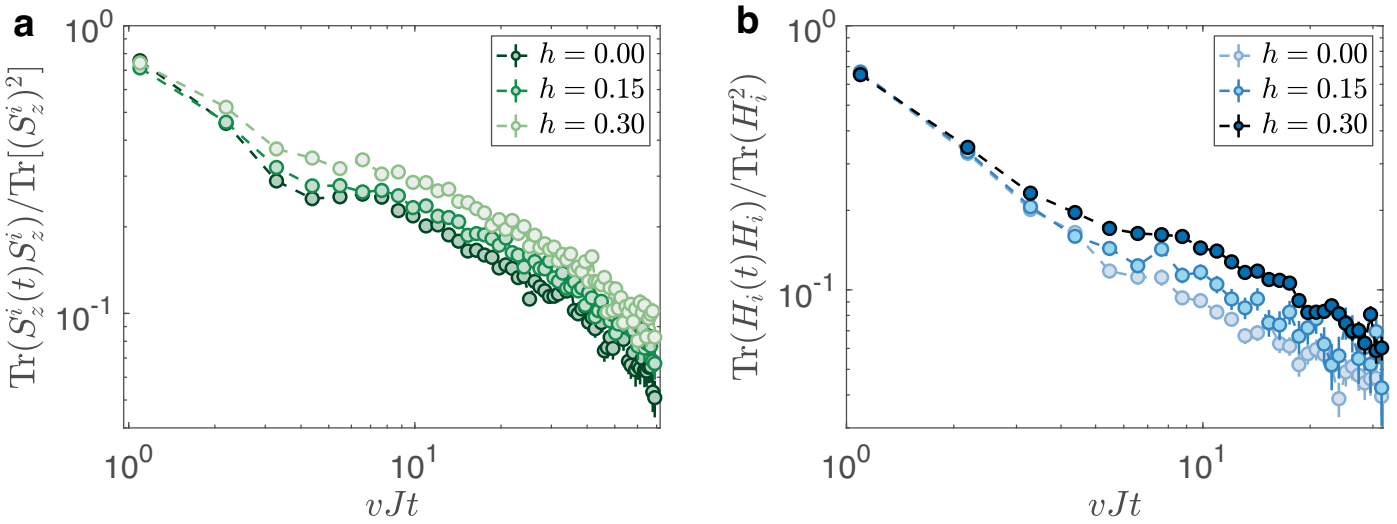

Extended Data Fig. 2 | Raw data for transport with disorder. Spin (**a**) and energy (**b**) autocorrelation for various disorder field strength h. Data are presented as mean values +/- SD from readout noise (for additional details see the Supplementary Information).